

Orthogonal beam-focusing with planar arrays for multiple access in near-field communications

Sotiris Droulias and Angeliki Alexiou, *Member, IEEE*

Abstract—Far-field multiple access techniques, such as space division multiple access (SDMA), leverage the angular orthogonality of beams in the far-field to serve multiple users with minimum interference. Recent approaches to extend this idea into the near-field involve the use of uniform planar arrays (UPAs) to generate focused beams that are able to achieve orthogonality only asymptotically, i.e. for infinitely large transmitter sizes. Gaining access to strictly zero beam correlations with transmitters of finite size could therefore lead to the full suppression of interference in the near-field, boosting the multiple access to unprecedented performance levels. In this work, we propose the use of circular, instead of the widely used rectangular, UPAs to generate focused beams that have strictly zero correlations. We demonstrate analytically that such beams satisfy the orthogonality condition for finite-size transmitters, thus offering a multitude of communication modes for multiple access in the near-field. We prove theoretically that focused beam orthogonality, defined in terms of the inner product of beam-focusing steering vectors, guarantees that the maximum of one beam is co-located with nulls of all other beams, similarly to how the angular orthogonality of classical far-field SDMA guarantees interference suppression. Based on this property, we propose codebook designs for near-field SDMA (NF-SDMA), which we evaluate in different scenarios. Our simulation results verify that the spectral efficiency of NF-SDMA schemes based on the proposed beams can be significantly higher than that achieved by focused beams generated with rectangular arrays.

I. INTRODUCTION

MULTIPLE access offers the advantage of having several users simultaneously served with minimum interference and optimal resource allocation. It relies on the orthogonality of beams, a key element for successfully retrieving the information assigned to different beams, even though they may coexist. For example, in classical far-field space division multiple access (SDMA) [1] it is possible to distinguish multiple users at different angles, due to the angular orthogonality of the beams.

Yet, with the gradual shift of wireless connectivity to higher frequencies, communications enter operation in the radiating near-field of antennas, rendering the applicability of well-known far-field multiple access schemes questionable. In view of the high requirements of future wireless connectivity [2], the utilization of frequency bands, such as the mmWave and THz, is gradually becoming common ground [3], [4], where new electrically large radiating elements are introduced, such as reconfigurable intelligent surfaces (RISs) [5]–[8], large antenna arrays (LAAs) and extremely large-scale antenna

arrays (ELAAs), equipped with many antenna elements [9]–[11]. With such large radiating apertures, the wavefront of the radiated wave can be tailored to acquire curvature beyond the typical far-field planar form, enabling beams that can focus, bend and even self-heal after encountering blockage [12]–[16].

Beam-focusing, in particular, is constantly gaining ground as a key element for energy-efficient communications [17]–[22] and localization applications [23]–[26]. Because of their unique ability to concentrate the power at desired distances and directions, focused beams offer controlled operation over the range-angle domain. Hence, as wireless connectivity is gradually shifting from the far-field to the radiating near-field of large radiating apertures, the design of orthogonal focused beams could bring the merits of classical far-field SDMA into the radiating near-field.

A. Prior works

In [27] it was recently shown that beam orthogonality, defined by means of the inner product of steering vectors, is preserved from the transmitter (Tx) to the receiver (Rx), regardless of the exact beam type. A novel technique for near-field SDMA (NF-SDMA) was introduced, which was based on cosine beams, a specially designed family of beams that ensure minimum interference, a necessary feature for serving multiple users equipped with multi-antenna or even single-antenna receivers. In [28] it was demonstrated how to construct communication modes with focused beams, by taking advantage of the narrow extent of the focal area. The proposed orthogonality ensured minimum interference between beams in the angular domain, similarly to how the maxima and minima of beams are treated in the classical far-field SDMA. In [29], a near-field non-orthogonal multiple access (NF-NOMA) scheme was proposed, which was based on beam-focusing, applied to users having different angular directions. It was demonstrated that the proposed NF-NOMA scheme improves the spectral efficiency compared to conventional far-field communications. In [30], [31], the concept of location division multiple access (LDMA) for single-antenna receivers was introduced, employing focused beams. It was shown that zero correlation between focused beams can be achieved only asymptotically, i.e. infinitely large arrays are required. Similarly, in [32], beam-focusing-based near-field multiple access schemes were analyzed, leveraging the angular orthogonality and the asymptotic range orthogonality of focused beams. In [33] it was recently shown that beam-focusing orthogonality is possible with uniform circular arrays (UCAs), i.e. linear arrays folded in a circular shape; however,

The authors are with the Department of Digital Systems, University of Piraeus, Piraeus 18534, Greece (Corresponding author: Sotiris Droulias, e-mail: sdroulias@unipi.gr)

Table I
SUMMARY OF PRIOR WORKS ON FOCUSED BEAM-BASED MULTIPLE ACCESS

Work	Array type	Focused beam orthogonality
[28]	ULA	angular only
[29]	ULA	non-orthogonal beams
[30]–[32]	ULA/UPA	asymptotic
[33]	UCA	for endfire beams only
[34]	UPA	OAM-enabled
this work	Circular UPA	angular and radial

all elements and users must be on the same plane and, hence, the waves generated from the back elements are interrupted from the front elements, with which they additionally interfere, rendering the practical and efficient formation of focused beams questionable. Last, in [34] the authors introduced orbital angular momentum (OAM) to achieve the generation of orthogonal focused beams with finite-size transmitters on the broadside. Yet, because the orthogonality derives entirely from the OAM, complex phase profiles are required. Table I summarizes the key aspects of the above prior works.

Evidently, with the exception of [27], the design of near-field multiple access schemes using uniform planar arrays (UPAs) relies primarily on the utilization of focused beams, which are either entirely non-orthogonal [29] or achieve orthogonality only asymptotically [30]–[32]. Hence, a multiple access scheme based on orthogonal beam-focusing with UPAs is still missing.

B. Our contributions

In this paper, we propose the concept of beam-focusing using circular UPAs, as a means to generate orthogonal beams that can serve as resource elements for near-field multiple access. The contributions are summarized as follows:

- We propose the concept of beam-focusing with circular UPAs, as a means to achieve focused beams with zero correlations. Beam correlations are defined as the inner product of the beam-focusing steering vectors.
- We derive analytically the correlations of focused beams, generated with rectangular and circular UPAs, and we provide analytical expressions for their orthogonality.
- We prove analytically that focused beams generated by circular arrays can be orthogonal for transmitters of finite size, contrary to focused beams generated by rectangular arrays, which are orthogonal only asymptotically, i.e. for transmitters of infinite size. For the former beams, there is a countable set of orthogonal beams, all propagating along the same direction and focusing at different distances from the transmitter. This property does not hold for the latter beams.
- We prove theoretically that beam orthogonality, i.e. zero inner product of the beam-focusing steering vectors, guarantees that the maximum of one beam is co-located with a null of all other beams, similarly to how the angular orthogonality of classical far-field SDMA guarantees interference suppression.

- Based on the beam orthogonality property, we propose codebook designs for NF-SDMA, using the class of focused beams generated by circular arrays that offer strictly zero correlations for transmitters of finite size, with respect to all associated parameters, such as the beam direction and focal distance.
- Our simulation results verify that the spectral efficiency of NF-SDMA schemes based on the proposed beams can be significantly higher than that achieved by focused beams generated with rectangular arrays.

C. Organization and notations

In Section II we introduce the system model for beam-focusing with rectangular and circular UPAs. In Section III we study the correlations of the two classes of focused beams and we demonstrate the orthogonality of the focused beams generated with circular arrays. In Section IV we propose codebook designs for multiple access in the near-field. In Section V we present the performance analysis and in Section VI we summarize the concluding remarks of this work.

Notations: In this paper \mathbb{Z} denotes the set of integers. $[\cdot]^T$ and $[\cdot]^H$ denote the transpose and conjugate-transpose operations, respectively; $\lfloor \cdot \rfloor$ is the floor function, $|\cdot|$ denotes the norm of its complex argument and the asterisk $*$ denotes the complex conjugate.

II. SYSTEM MODEL

Let us consider a large UPA, centered at the origin of the coordinate system and extending on the xy -plane, as depicted in Fig. 1(a). The UPA consists of $N_x \times N_y$ elements with spacing l_x and l_y along the x and y directions, respectively, and has size $L_x \times L_y$, i.e. $L_x = N_x l_x$ and $L_y = N_y l_y$. The UPA generates beams with tailored amplitude and phase characteristics that propagate in the $z > 0$ semi-infinite space. The E -field profile at the UPA ($z = 0$) has the form

$$E(x, y) = A(x, y)e^{j\phi(x, y)}, \quad (1)$$

where A is the amplitude and ϕ the phase. As, for several applications, it is convenient to have uniform amplitude, throughout this work we will use constant $A(x, y) = 1$ V/m in all examples. The coordinates x, y are continuous and, hence, only the discrete locations $x = n_x l_x$, $y = n_y l_y$ with $n_x, n_y \in \mathbb{Z}$ are implied in (1).

For beam-focusing, the UPA elements create spherical wavefronts, which cause all rays from the UPA to converge at the desired focal distance f_0 , as depicted in Fig. 1(a). To steer the focused beam along the direction θ_r on the xz -plane, the UPA phase must be of the form [13], [14]

$$\phi(x, y) = k\sqrt{(x - f_0 \sin \theta_r)^2 + y^2 + (f_0 \cos \theta_r)^2}, \quad (2)$$

where $k = 2\pi/\lambda$ is the free-space wavenumber and λ the wavelength.

An example phase profile is shown in Fig. 1(b), for $\theta_r = 0^\circ$, $f_0 = 10$ m. The spherical phase profile has been folded within the $(-\pi, \pi)$ range and the amplitude is uniform throughout the

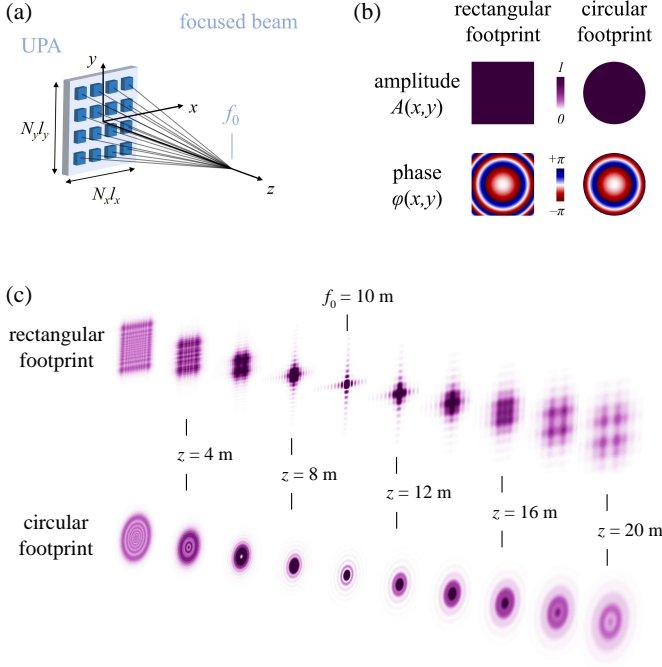


Figure 1. Focused beam generation with UPAs. (a) Representation of focused beam as rays traveling from the UPA and converging at the focal distance f_0 . (b) Amplitude and phase of UPA elements, for rectangular and circular beam footprint. (c) Numerical propagation of focused beam with $f_0 = 10$ m, using all the elements of the UPA (top) and a sub-array selection to form a disk (bottom). The UPA operates at 150 GHz ($\lambda = 2$ mm) and consists of 500×500 elements, equally spaced by $L_x = L_y = \lambda/2$.

entire UPA area. For rectangular UPA, the beam's footprint extends across the entire rectangular area $L_x \times L_y$; for circular UPA the beam's footprint is limited within the disk of diameter $L \equiv L_x = L_y$. The shape of the footprint only qualitatively determines how the beam power density is redistributed along its propagation, while the focusing location, which is characterized by the parameters θ_r , f_0 , is entirely controlled via the phase of the footprint. This is demonstrated in Fig. 1(c), where the beams that correspond to the individual footprints of Fig. 1(b) are propagated numerically (see Appendix VI-A for details). Note how, despite their qualitatively different features, both beams concentrate their power at the intended location ($x = 0$, $y = 0$, $z = f_0$). In this example the UPA consists of 500×500 elements. The operation frequency is 150 GHz ($\lambda = 2$ mm) and the UPA elements are equally spaced by $L_x = L_y = \lambda/2$, throughout all the examples in this work.

III. FOCUSED BEAM ORTHOGONALITY

To construct codebooks for NF-SDMA, we first need to investigate under which circumstances the maximum of a focused beam can be co-located with nulls of all other focused beams. To this end, we start by analyzing how the power at the Rx location is associated with the beam orthogonality at the Tx, which is defined by means of the inner product of the beam-focusing steering vectors.

A. NEAR-FIELD CHANNEL MODELING

Consider a Tx equipped with a UPA, consisting of N elements with coordinates (x_n, y_n, z_n) , $n = 1, 2, \dots, N$. The Tx is communicating with multiple Rx's, located at (x_m, y_m, z_m) , $m = 1, 2, \dots, M$. The steering vector of the UPA is written as $\mathbf{w} = [w_1, w_2, \dots, w_N]^T$, with entries

$$w_n = A_n \exp(j\phi_n), \quad (3)$$

where A_n is the amplitude and ϕ_n is the phase of the n^{th} element. As shown in Appendix VI-A, the line-of-sight (LoS) channel between the n^{th} element of the Tx and the m^{th} Rx is

$$h_{mn} = \frac{\exp(-jkd_{mn})}{d_{mn}}, \quad (4)$$

where $d_{mn} = \sqrt{(x_n - x_m)^2 + (y_n - y_m)^2 + (z_n - z_m)^2}$ is the distance between the n^{th} Tx element and the m^{th} Rx. All things considered, the E -field at the m^{th} Rx, due to the radiated power from the Tx, is expressed as

$$E_m = \sum_n h_{mn} w_n + v_m, \quad (5)$$

where v_m is the noise at the m^{th} Rx.

For steering vectors with uniform amplitude, we may set $A_1 = A_2 = \dots = A_N \equiv A_0$. Additionally, for operation in the radiating near-field, yet relatively far from the Tx, we may approximate $d_{m1} = d_{m2} = \dots = d_{mN} \approx d_R$ for the $1/d_{mn}$ term in (4). In this case, (5) is written in compact form as

$$E_m = \frac{A_0}{d_R} \sqrt{N} \sqrt{N} \mathbf{a}_h^H \mathbf{a}_w + v_m, \quad (6)$$

with

$$\mathbf{a}_h = \frac{1}{\sqrt{N}} [e^{j\psi_1}, e^{j\psi_2}, \dots, e^{j\psi_N}]^T, \quad (7a)$$

$$\mathbf{a}_w = \frac{1}{\sqrt{N}} [e^{j\phi_1}, e^{j\phi_2}, \dots, e^{j\phi_N}]^T, \quad (7b)$$

and $\psi_n = kd_{mn}$, i.e.

$$\psi_n = k\sqrt{(x_n - x_m)^2 + (y_n - y_m)^2 + (z_n - z_m)^2}. \quad (8)$$

Note that, while h_{mn} in (4) is associated with the radiated field of a single array element, E_m in (5) expresses the collective response from all elements. Hence, while h_{mn} is agnostic of L (which expresses the number of all elements) and f_0 , θ_r (which express their relative phases), the total field E_m depends on all three parameters.

B. BEAM CORRELATIONS AND NF-SDMA

Depending on the functional form of ϕ_n , the steering vector phase, different types of beams can be generated (e.g., focused [13], [14], bending [16], [35], cosine [27]). While ϕ_n in (7b) can take any desired form, ψ_n in (7a) is always given by (8) and, therefore, ϕ_n and ψ_n are generally different. Note, however, that specifically for beam-focusing, the functional form of ϕ_n becomes identical to that of ψ_n , simply because focusing requires the formation of spherical wavefronts, which

are exactly what the term h_{mn} represents. This becomes apparent when comparing ψ_n in (8) with

$$\phi_n = k \sqrt{(x_n - f_0 \sin \theta_r)^2 + y_n^2 + (f_0 \cos \theta_r)^2}, \quad (9)$$

which is (2), calculated at the Tx element locations.

In view of this observation, consider two focused beams, A and B, with properties $(\theta_{r,A}, f_{0,A})$ and $(\theta_{r,B}, f_{0,B})$, respectively, corresponding to the steering vector phases $\phi_{n,A}$ and $\phi_{n,B}$. To construct the steering vectors $\mathbf{a}_{w,A}$ and $\mathbf{a}_{w,B}$ that generate these beams we use (7b) with $\phi_{n,A}$ and $\phi_{n,B}$, given by (9). Then, the inner product of the steering vectors will be $\mathbf{a}_{w,A}^H \mathbf{a}_{w,B}$. Due to the identical functional form of (8) and (9), $\mathbf{a}_{w,A}^H \mathbf{a}_{w,B}$ is equivalent to the inner product $\mathbf{a}_h^H \mathbf{a}_w$ in (6), if we set $\psi_n \equiv \phi_{n,A}$ and $\phi_n \equiv \phi_{n,B}$; this corresponds to calculating the E -field of beam B at location $(x_m = f_{0,A} \sin \theta_{r,A}, y_m = 0, z_m = f_{0,A} \cos \theta_{r,A})$. As a result, because the nulls of $\mathbf{a}_{w,A}^H \mathbf{a}_{w,B}$ will be also nulls of $\mathbf{a}_h^H \mathbf{a}_w$, zero correlations of the steering vectors $\mathbf{a}_{w,A}$ and $\mathbf{a}_{w,B}$ will correspond to locations $(x_m = f_{0,A} \sin \theta_{r,A}, y_m = 0, z_m = f_{0,A} \cos \theta_{r,A})$ where (6) yields $E_m = 0$. Hence, the focal point of beam A will be at a location where beam B has a null.

Using a different beam A leads to different nulls of beam B and, after scanning the entire parametric space, a beamset is formed, containing all beams that are orthogonal to beam B. If all beams belonging to the beamset are mutually orthogonal, this means that at the focal point of any beam all other beams will be null. Consequently, the orthogonality of the beam-focusing steering vectors, defined in terms of their inner product, guarantees that the maximum of one beam will be co-located with a null of another beam, exactly as occurs with classical far-field SDMA in the angular domain (see Appendix VI-B for details); hence the term NF-SDMA. In view of this property, the task of devising NF-SDMA codebooks simply translates into identifying the combinations of beam-focusing steering vector pairs that yield zero inner product.

C. BEAM-FOCUSING STEERING VECTOR ORTHOGONALITY

To identify the combinations of beam-focusing steering vector pairs that yield zero inner product, consider a focused beam with tunable parameters θ_r, f_0 , and a reference beam with fixed parameters $\theta_{r,\text{ref}}, f_{0,\text{ref}}$, as depicted in Fig. 2(a). The inner product of the two beams is expressed as [27]

$$C = \left| \frac{\iint E_{\text{ref}}(x, y) E^*(x, y) dx dy}{\sqrt{\iint |E_{\text{ref}}(x, y)|^2 dx dy} \sqrt{\iint |E(x, y)|^2 dx dy}} \right|, \quad (10)$$

where $E_{\text{ref}}(x, y) = \exp(j\phi_{\text{ref}}(x, y))$ and $E(x, y) = \exp(j\phi(x, y))$ are the footprints of the two beams at the Tx, with ϕ_{ref} (involving $\theta_{r,\text{ref}}, f_{0,\text{ref}}$) and ϕ (involving θ_r, f_0) given by (2). The integration is performed within the area of the UPA, outside of which the footprints are zero, i.e. $|x| < L_x/2, |y| < L_y/2$ for rectangular UPA of size $L_x \times L_y$, and $x^2 + y^2 < (L/2)^2$ for circular UPA of diameter $L \equiv L_x = L_y$. Without loss of generality we consider UPAs with equally spaced elements, i.e. $l_x = l_y \equiv l$.

To cast (10) in analytical form, (2) can be simplified by

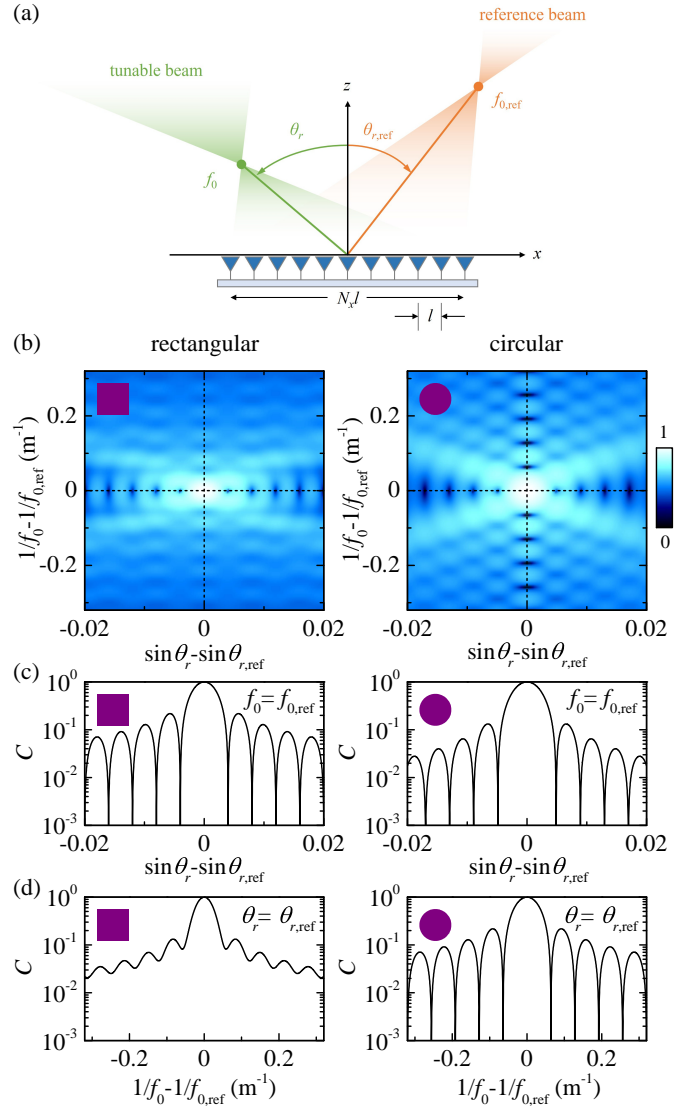


Figure 2. Correlation of focused beams. (a) System model for UPA communication systems, depicting a xz -cross section of two focused beams with parameters (θ_r, f_0) and $(\theta_{r,\text{ref}}, f_{0,\text{ref}})$, respectively. (b) Plots of C , as a function of the detuning parameters $w_\theta/kl = \sin \theta_r - \sin \theta_{r,\text{ref}}$ and $w_f/kl^2 = 1/f_0 - 1/f_{0,\text{ref}}$, for a UPA with $N_x = N_y = 500$ elements. Left panel: rectangular UPA. Right panel: circular UPA. The color plots are depicted in log scale, to emphasize the details. (c) Cross-section of C at the characteristic detuning $w_f = 0$. (d) Cross-section of C at the characteristic detuning $w_\theta = 0$. The cross-sections are marked in (b) with the dashed lines.

taking advantage of the relatively large curvature of the phase, required to focus the beam at distances larger than the RIS size. Expanding (2) around the center of the UPA, i.e. at $x = 0, y = 0$, and keeping all terms up to 2^{nd} order leads to

$$\phi(x, y) = -kx \sin \theta_r + k \frac{x^2 \cos^2 \theta_r + y^2}{2f_0}. \quad (11)$$

As we show analytically in Appendix VI-C, the parabolic phase (11) is a valid approximation of the exact spherical phase profile (2) for a wide range of practical cases. In the limit $f_0 \rightarrow \infty$, (11) becomes $\phi(x, y) = -kx \sin \theta_r$, i.e. approaches the

Table II
SUMMARY OF DETUNING PARAMETERS

Parameter	Description	Equation
w_θ	Detuning of angles $\theta_r, \theta_{r,\text{ref}}$	(13a)
w_f	Detuning of focal distances $f_0, f_{0,\text{ref}}$	(13b)

phase for conventional beamsteering [13], [14]. In essence, the linear term in (11) accounts for steering and the nonlinear term for focusing.

Using (11), the correlation function (10) takes the form

$$C(w_\theta, w_f) = \frac{1}{S_{\text{UPA}}} \left| \iint e^{jw_\theta \left(\frac{x}{l}\right)} e^{-\frac{j}{2}w_f \left[\left(\frac{x}{l}\right)^2 \delta_\theta + \left(\frac{y}{l}\right)^2\right]} dx dy \right|, \quad (12)$$

where

$$w_\theta = kl(\sin \theta_r - \sin \theta_{r,\text{ref}}), \quad (13a)$$

$$w_f = kl \left(\frac{l}{f_0} - \frac{l}{f_{0,\text{ref}}} \right), \quad (13b)$$

are dimensionless parameters that express the angular detuning and focal distance detuning, respectively, between the two beams, and

$$\delta_\theta = \frac{f_0 \cos^2 \theta_{r,\text{ref}} - f_{0,\text{ref}} \cos^2 \theta_r}{f_0 - f_{0,\text{ref}}}. \quad (14)$$

The detuning parameters w_θ and w_f are summarized in Table II. S_{UPA} is the UPA area, i.e. $S_{\text{UPA}} = L_x L_y$ for rectangular UPA and $S_{\text{UPA}} = \pi L^2/4$ for circular UPA.

The correlation function C is demonstrated in Fig. 2(b) for relatively small angles, where $\delta_\theta \approx 1$, as a function of the detuning parameters $w_\theta/kl = \sin \theta_r - \sin \theta_{r,\text{ref}}$ and $w_f/kl^2 = 1/f_0 - 1/f_{0,\text{ref}}$. The UPA has $N_x = N_y = 500$ elements, which are all used in the left panel, while a circular sub-array selection is used in the right panel, to form a circular UPA. The color plots are depicted in log scale, to emphasize the details. Clearly, in the examined parametric space, $C = 0$ can be achieved with both UPAs, as long as $f_0 = f_{0,\text{ref}}$ and $\theta_r \neq \theta_{r,\text{ref}}$, i.e. if both beams are focused at the same distance, along different directions. This is explicitly shown in the panels of Fig. 2(c), which correspond to the horizontal cross-sections marked with the dashed lines in Fig. 2(b). However, for beams focused along the same direction, i.e. with $\theta_r = \theta_{r,\text{ref}}$ and $f_0 \neq f_{0,\text{ref}}$, $C > 0$ for the rectangular UPA, while $C = 0$ is achieved with the circular UPA, at distinct focal distances. This is demonstrated in the panels of Fig. 2(d), which correspond to the vertical cross-sections marked with the dashed lines in Fig. 2(b).

Note that, while C results from integration on a continuous aperture, for densely spaced elements (e.g., such as $l = \lambda/2$, as considered here), summation of the integrand in (12) over the UPA discrete element locations leads to approximately the same result. Hence, in what follows, we use (12) to analytically calculate the beam correlations for the two characteristic cases, namely $w_\theta \neq 0, w_f = 0$ and $w_\theta = 0, w_f \neq 0$, and subsequently substitute $L_x \rightarrow N_x l, L_y \rightarrow N_y l$ in the result, to account for the discrete UPA character.

D. BROADSIDE BEAMS WITH COMMON FOCAL DISTANCE

This case refers to beams with $w_\theta \neq 0$ and $w_f = 0$, for which $\theta_r, \theta_{r,\text{ref}} \approx 0^\circ$, i.e. $\delta_\theta \approx 1$. For rectangular UPA, integration of (12) with $w_f = 0$ and $\delta_\theta = 1$ leads to

$$C_{\text{rect}}(w_\theta, 0) = \left| \frac{\sin\left(\frac{N_x}{2} w_\theta\right)}{\frac{N_x}{2} w_\theta} \right|, \quad (15)$$

where the subscript *rect* denotes the rectangular shape of the UPA. The solutions of equation $C_{\text{rect}}(w_\theta, 0) = 0$ satisfy

$$w_\theta = \frac{2\pi q}{N_x}, \quad (16)$$

where $q \in \mathbb{Z}$, with $q \neq 0$, to exclude the nulls of the denominator that lead to $C_{\text{rect}}(w_\theta, 0) = 1$. As dictated by (13a), $|w_\theta| \leq 2kl$, which according to (16) leads to $|q| \leq N_x kl/\pi$, and hence $0 < |q| \leq N_x kl/\pi$. In Fig. 2(c), left panel, the first few nulls of C_{rect} with $q = \pm 1, \dots, \pm 5$ are visible.

For circular UPA, integration of (12) with $w_f = 0$ and $\delta_\theta = 1$ leads to

$$C_{\text{circ}}(w_\theta, 0) = 2 \left| \frac{J_1\left(\frac{N}{2} w_\theta\right)}{\frac{N}{2} w_\theta} \right|, \quad (17)$$

where $N \equiv N_x = N_y$, $J_\alpha(\cdot)$ is the Bessel function of the first kind with $\alpha = 1$, and the subscript *circ* denotes the circular shape of the UPA. The solutions of equation $C_{\text{circ}}(w_\theta, 0) = 0$ satisfy

$$w_\theta = \frac{2r_q}{N}, \quad (18)$$

where $r_q, q \in \mathbb{Z}$, are the roots of $J_1(r_q) = 0$. From the solution set (18) only $q = 0$ lifts the orthogonality and, following the same reasoning as with C_{rect} , the nulls of C_{circ} are limited within the values $0 < |r_q| \leq Nkl$. The first few nulls of C_{rect} with $q = \pm 1, \dots, \pm 5$ are visible in Fig. 2(c), right panel.

E. BROADSIDE BEAMS WITH COMMON DIRECTION

This case refers to beams with $w_\theta = 0$ and $w_f \neq 0$, for which $\theta_r, \theta_{r,\text{ref}} \approx 0^\circ$, i.e. $\delta_\theta \approx 1$. For rectangular UPA, integration of (12) with $w_\theta = 0$ and $\delta_\theta = 1$ leads to

$$C_{\text{rect}}(0, w_f) = \frac{2\pi}{N_x N_y w_f} \times \left| \text{erf}\left(\frac{1+j}{4} N_x \sqrt{w_f}\right) \text{erf}\left(\frac{1+j}{4} N_y \sqrt{w_f}\right) \right|, \quad (19)$$

where $\text{erf}(\cdot)$ is the error function. Because the function $\text{erf}(r)/r$ is nonzero, $C_{\text{rect}}(0, w_f)$ does not have nulls and, hence, focused beams along the same direction cannot be orthogonal. Although this conclusion has been drawn for small angles, this is a general result, and applies to any angles, as shown in Appendix VI-D.

Note that, because $r \rightarrow \infty \Rightarrow \text{erf}(r)/r \rightarrow 0$, $C_{\text{rect}}(0, w_f)$ becomes asymptotically zero for large N_x, N_y . Hence, beams focused along the same direction can become asymptotically orthogonal for large UPA size. As an example, in Fig. 3(a), left panel, C_{rect} is presented as a function of the UPA size, and the detuning parameter $w_f/kl^2 = 1/f_0 - 1/f_{0,\text{ref}}$. A cross-section at $1/f_0 - 1/f_{0,\text{ref}} = 0.1 \text{ m}^{-1}$ is marked with the dashed

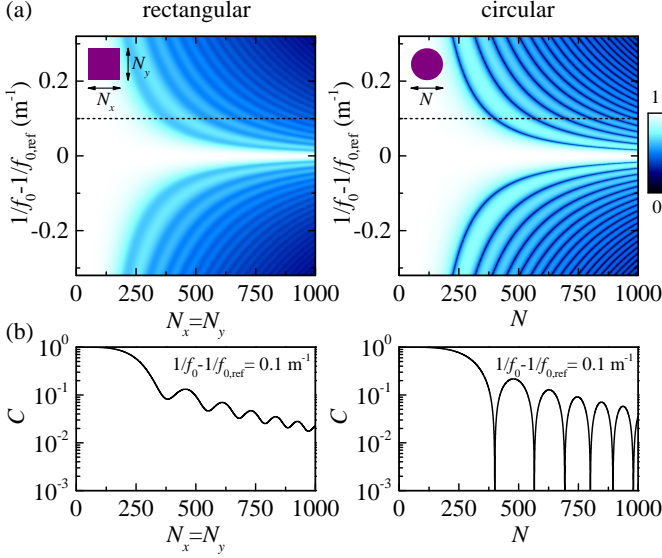


Figure 3. From asymptotic to full orthogonality. (a) Beam correlations, as a function of the UPA size $N_x = N_y \equiv N$, and the detuning parameter $1/f_0 - 1/f_{0,\text{ref}}$, for beams propagating along a common direction with $\theta_r = \theta_{r,\text{ref}} = 0^\circ$. *Left panels*: rectangular UPA. *Right panels*: circular UPA. The color plots are depicted in log scale, to emphasize the details. (b) Cross-sections of C at $1/f_0 - 1/f_{0,\text{ref}} = 0.1 \text{ m}^{-1}$ for both UPAs. The cross-sections are marked in (a) with the dashed lines.

line and is shown explicitly in Fig. 3(b), left panel. Note how increasing the UPA size leads gradually to $C_{\text{rect}} \rightarrow 0$, as also demonstrated in [30], [31].

For circular UPA, integration of (12) with $w_\theta = 0$ and $\delta_\theta = 1$ leads to

$$C_{\text{circ}}(0, w_f) = \left| \frac{\sin\left(\frac{N^2}{16} w_f\right)}{\frac{N^2}{16} w_f} \right|. \quad (20)$$

Equation $C_{\text{circ}}(0, w_f) = 0$ has roots

$$w_f = \frac{16\pi p}{N^2}, \quad (21)$$

where $p \in \mathbb{Z}$, with $p \neq 0$, to exclude the nulls of the denominator that lead to $C_{\text{circ}}(0, w_f) = 1$, hence $|p| > 0$. The first few nulls of $C_{\text{circ}}(0, w_f)$ with $p = \pm 1, \dots, \pm 4$ can be identified in Fig. 2(d), right panel.

In Fig. 3(a), right panel, C_{circ} is presented as a function of the UPA size, and the detuning parameter $w_f/kl^2 = 1/f_0 - 1/f_{0,\text{ref}}$. Contrary to C_{rect} , the correlations acquire zeros, which are explicitly shown in Fig. 3(b), right panel, for the cross-section marked with the dashed line.

All orthogonality conditions are summarized in Table III.

F. ORTHOGONALITY BEYOND THE BROADSIDE

In Sections III-D and III-E we demonstrated that circular UPAs support orthogonal, focused beams for relatively small steering angles. Although the orthogonality breaks for generally different angles and different focal distances, there are two characteristic cases for which it can be preserved at larger steering angles, beyond the broadside.

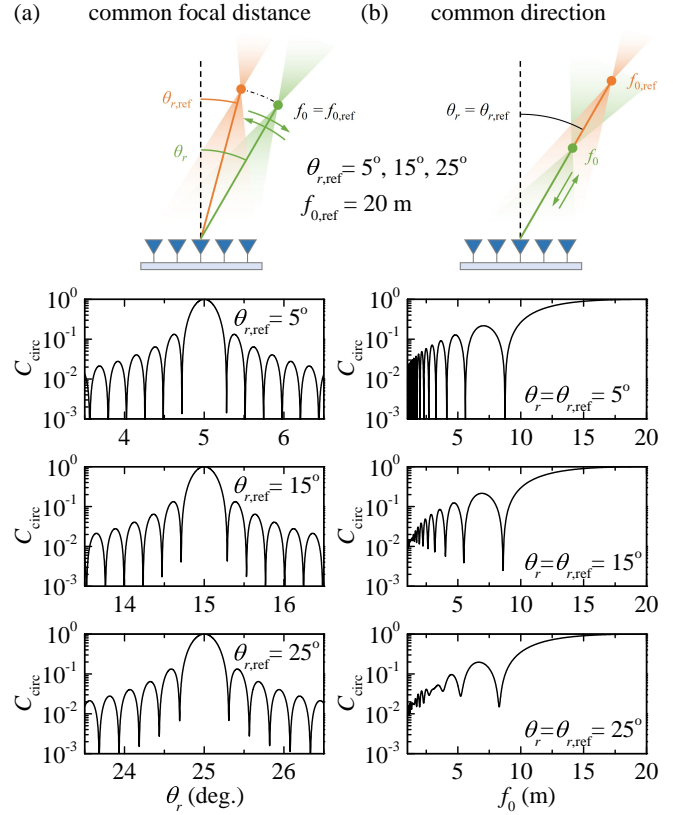


Figure 4. Focused beam orthogonality with circular UPAs, beyond the broadside. (a) Correlation of beams with common focal distance $f_0 = f_{0,\text{ref}} = 20 \text{ m}$. The direction of the tunable beam varies within a range of $\pm 1.5^\circ$ around the direction of the reference beam, for $\theta_{r,\text{ref}} = 5^\circ, 15^\circ, 25^\circ$. (b) Correlation of beams with common direction $\theta_r = \theta_{r,\text{ref}} = 5^\circ, 15^\circ, 25^\circ$. The reference beam is focused at $f_{0,\text{ref}} = 20 \text{ m}$ and the tunable beam within the range 1 – 20 m.

1) *Beams with common focal distance*: In this case (14) becomes $\delta\theta = \cos^2 \theta_{r,\text{ref}} - \cos^2 \theta_r$, i.e. the orthogonality can be preserved at arbitrarily large angles, as long as $\theta_{r,\text{ref}} \approx \theta_r$. Hence, beams with the same focal distance that are directed towards close-by angles are expected to achieve strictly zero correlations. This is demonstrated in Fig. 4(a), where $f_0 = f_{0,\text{ref}} = 20 \text{ m}$, and the direction of the tunable beam varies within a range of $\pm 1.5^\circ$ around the direction of the reference beam. In these examples, the beam correlations are studied for $\theta_{r,\text{ref}} = 5^\circ$, $\theta_{r,\text{ref}} = 15^\circ$ and $\theta_{r,\text{ref}} = 25^\circ$.

2) *Beams with common direction*: In this case (14) becomes $\delta\theta = \cos^2 \theta_r$, which is independent of the focal distance. This is demonstrated in Fig. 4(b), where the beams are focused

Table III
SUMMARY OF FOCUSED BEAM ORTHOGONALITY CONDITIONS

UPA	Beam detuning	Orthogonality condition	Mode enumeration
rectangular	$w_f = 0$	$w_\theta = \frac{2\pi q}{N_x}$; (16)	$0 < q \leq N_x kl / \pi$
	$w_\theta = 0$	-	-
circular	$w_f = 0$	$w_\theta = \frac{2\pi q}{N}$; (18)	$0 < q \leq N kl$
	$w_\theta = 0$	$w_f = \frac{16\pi p}{N^2}$; (21)	$ p > 0$

along a common direction, according to the values of the previous example, i.e. $\theta_r = \theta_{r,\text{ref}} = 5^\circ, 15^\circ, 25^\circ$. The reference beam is focused at $f_{0,\text{ref}} = 20$ m and the tunable beam within the range 1 – 20 m. As expected, with increasing angle, the orthogonality gradually breaks. Yet, for a large angular range, C_{circ} is preserved at relatively low values, giving promise for efficient suppression interference, even at such non-ideal cases.

IV. CODEBOOK DESIGN FOR CIRCULAR UPA'S

To design codebooks for near-field multiple access, sets of orthogonal beams are required, i.e. beams with properties that correspond to the nulls of C for any pair combination. Next, we will show that, for focused beams generated with circular UPAs, all beams with $w_f = 0$ and w_θ given by (18) are orthogonal, and that the same property holds for all beams with $w_\theta = 0$ and w_f given by (21).

A. BEAMSET ORTHOGONALITY

For the beamset with $w_\theta = 0$ and $w_f \neq 0$ we have found that the nulls of C_{circ} are given by (21). Using (13b), we can determine all beams that are orthogonal to the reference beam. These beams are characterized by the focal distance

$$f_0 = \left(\frac{1}{f_{0,\text{ref}}} + \frac{\pi}{kl} \frac{16p}{N^2 l} \right)^{-1}, \quad (22)$$

with $p \in \mathbb{Z}_{\neq 0}$. The values of p in (22) defines a beamset, where all beams are orthogonal to the reference beam. Hence, we can select two beams A and B for two different integers p_A and p_B , so that each is orthogonal to the reference beam, satisfying (21), i.e.

$$kl \left(\frac{l}{f_{0,A}} - \frac{l}{f_{0,\text{ref}}} \right) = \frac{16\pi p_A}{N^2}, \quad (23a)$$

$$kl \left(\frac{l}{f_{0,B}} - \frac{l}{f_{0,\text{ref}}} \right) = \frac{16\pi p_B}{N^2}, \quad (23b)$$

where $f_{0,A}$ and $f_{0,B}$ are the individual focal distances, and the beams propagate along the same direction as the reference beam. Eliminating $f_{0,\text{ref}}$ from (23a),(23b) leads to

$$kl \left(\frac{l}{f_{0,A}} - \frac{l}{f_{0,B}} \right) = \frac{16\pi(p_A - p_B)}{N^2}, \quad (24)$$

where $p_A - p_B$ is also an integer and, therefore, beams A and B satisfy (21). Because beams A and B are different, $p_A - p_B$ is nonzero, ensuring that the denominator in (20) is nonzero, i.e. $C_{\text{circ}} \equiv 0$. As a result, because the chosen beams can be any pair belonging to the beamset, (21) guarantees that all beams are orthogonal. For the beamset with $w_\theta \neq 0$, $w_f = 0$ the proof follows similar steps.

B. CODEBOOKS AND MODE ENUMERATION

Based on the beam orthogonality that characterizes each beamset of Table III, we can construct two sets of relevant codebooks, which we refer to as $\text{CB}f_n$ and $\text{CB}\theta_n$.

Codebook $\text{CB}f_n$ contains all focused beams with the same focal distance $f_0 = f_{0,\text{ref}} \equiv f_n$ and different steering angles. The subscript n denotes the n^{th} version of the codebook, in which

all beams are characterized by the same f_n . The orthogonal beam directions are found by expressing the solution (18) in terms of θ_r , using (13a), i.e.

$$\theta_r = \arcsin \left(\frac{2r_q}{Nkl} \right). \quad (25)$$

Without loss of generality, we have used $\theta_{r,\text{ref}} = 0^\circ$ for the reference beam. The steering angles in (25) provide the orthogonal beam entries of $\text{CB}f_n$, i.e. the near-field communication modes with common focal distance f_n . The maximum number of codebook entries depends on the maximum steering angle, $\theta_{r,\text{max}}$, which is chosen at will. To identify all such beam directions we need to solve (25) for $|\theta_r| \leq \theta_{r,\text{max}}$. At this point, we may use a 1st order approximation to the roots of $J_1(r_q)$, which reads as $r_q \approx \pi(4q+1)/4$. Then, the maximum integer, $q_{\text{max}} = \max(|q|)$, that satisfies $|\theta_r| \leq \theta_{r,\text{max}}$ is expressed analytically as

$$q_{\text{max}} = \left\lfloor \sin(\theta_{r,\text{max}}) \frac{L}{\lambda} - \frac{1}{4} \right\rfloor, \quad (26)$$

yielding a total of $2q_{\text{max}} + 1$ orthogonal beams ($q = -q_{\text{max}}, \dots, 0, \dots, q_{\text{max}}$), i.e. communication modes. The maximum number of codebook $\text{CB}f_n$ entries is presented in Fig. 5(a), as a function of the UPA size. The orange dot marks the case for $N = 500$ and $\max(\theta_r) = 2.5^\circ$.

Codebook $\text{CB}\theta_n$ contains all focused beams with the same steering angle $\theta_r = \theta_{r,\text{ref}} \equiv \theta_n$ and different focal distances. The subscript n denotes the n^{th} version of the codebook, in which all beams are characterized by the same θ_n . The orthogonal focal distances are found by are found by expressing the solution (21) in terms of $f_{0,\text{ref}}$, using (13b), which leads to (22). Without loss of generality, we may use $f_{0,\text{ref}} \rightarrow \infty$ for the reference beam, in which case the orthogonal beam entries of $\text{CB}\theta_n$, i.e. the near-field communication modes with common direction θ_n , are given by the focal distances

$$f_0 = \frac{kl}{\pi} \frac{N^2 l}{16p}. \quad (27)$$

The maximum number of codebook entries depends on the maximum range of focal distances. The maximum f_0 , i.e. $f_{0,\text{max}}$, is determined by (27) with $p = 1$, i.e. $f_{0,\text{max}} = N^2 l / 16$; the minimum f_0 is chosen at will and corresponds to a maximum p in (27). The maximum integer, $p_{\text{max}} = \max(|p|)$ that satisfies $f_{0,\text{min}} \leq f_0$ is found by solving (27) in terms of p , and is given by

$$p_{\text{max}} = \left\lfloor \frac{1}{8} \left(\frac{L}{\lambda} \right)^2 \left(\frac{f_{0,\text{min}}}{\lambda} \right)^{-1} \right\rfloor, \quad (28)$$

yielding a total of p_{max} orthogonal beams ($p = 1, 2, \dots, p_{\text{max}}$), i.e. communication modes. The maximum number of codebook $\text{CB}\theta_n$ entries is presented in Fig. 5(b), as a function of the UPA size. In the example marked with the orange dot, where $N = 500$, $f_{0,\text{max}} = 15.625$ m, and $f_{0,\text{min}} = 1$ m yields $p_{\text{max}} = 15$, i.e. there are 15 communication modes within the range 1 m – 15.625 m.

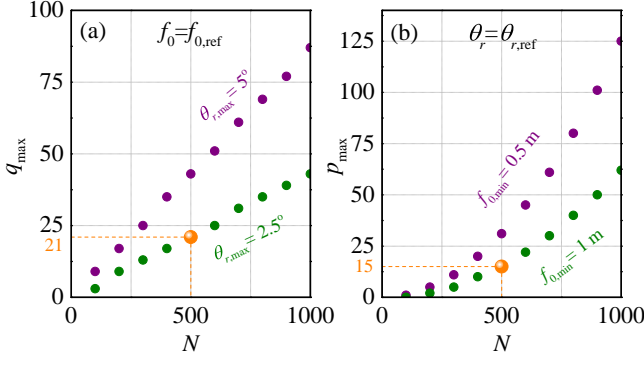


Figure 5. Maximum number of communication modes, as a function of the circular UPA size. (a) Modes of codebook CBf_n , which contains all beams with common focal distance $f_0 = f_{0,ref} \equiv f_n$, directed within the angular range $\theta_r \in [-\theta_{r,max}, +\theta_{r,max}]$. (b) Modes of $CB\theta_n$, which contains all beams with common direction $\theta_r = \theta_{r,ref} \equiv \theta_n$, focused within the focal distance range $f_0 \in [f_{0,min}, 16/N^2 l]$. The orange dots mark examples for $N = 500$.

C. UPA STEERING VECTORS

Once the steering angles and focal distances of all beams have been identified, next the steering vectors are constructed. To this end, we discretize the continuous phase on the UPA grid, i.e. we express (2) at points $x = n_x l_x, y = n_y l_y$. The discretized version of the UPA phase acquires the form

$$\phi(n_x, n_y) = k \sqrt{(n_x l_x - f_0 \sin \theta_r)^2 + (n_y l_y)^2 + (f_0 \cos \theta_r)^2}, \quad (29)$$

which is (9) expressed in terms of

$$n_x = -\frac{N_x - 1}{2}, -\frac{N_x - 1}{2} + 1, \dots, \frac{N_x - 1}{2}, \quad (30a)$$

$$n_y = -\frac{N_y - 1}{2}, -\frac{N_y - 1}{2} + 1, \dots, \frac{N_y - 1}{2}. \quad (30b)$$

The steering vector that imposes the phase profile (29) on the elements of the UPA, is given by

$$\mathbf{a}(\theta_r, f_0) = \frac{1}{\sqrt{N_x N_y}} \mathbf{a}_y(\theta_r, f_0)^T \otimes \mathbf{a}_x(\theta_r, f_0), \quad (31)$$

where the symbol \otimes denotes the Kronecker product, and

$$\mathbf{a}_x(\theta_r, f_0) = \left[e^{j\phi(-\frac{N_x-1}{2}, 0)}, e^{j\phi(-\frac{N_x-1}{2}+1, 0)}, \dots, e^{j\phi(\frac{N_x-1}{2}, 0)} \right], \quad (32a)$$

$$\mathbf{a}_y(\theta_r, f_0) = \left[e^{j\phi(0, -\frac{N_y-1}{2})}, e^{j\phi(0, -\frac{N_y-1}{2}+1)}, \dots, e^{j\phi(0, \frac{N_y-1}{2})} \right]. \quad (32b)$$

The full form of (31) provides the steering vector of the rectangular UPA. For the circular UPA only the subarray with $n_x^2 + n_y^2 \leq ((N-1)/2)^2$ is considered, where $N \equiv N_x = N_y$.

The codebook design steps are outlined in **Algorithm 1**.

V. PERFORMANCE ANALYSIS

Due to their unique ability to concentrate power in a small area, focused beams are ideal for serving users that are distributed at generally different angles with minimum

Algorithm 1 Codebook design

Codebook CBf_n

M : number of users \triangleright Same number of beams
 f_n : Choose common focal distance of M beams
 $q = 1$: First codeword index
 $q = M$: Last codeword index
while $q \leq M$ **do**
 Determine steering angles θ_r using (25).
 Create steering vector for q^{th} beam using (31)
 Fill in the q^{th} codebook entry
end while

Codebook $CB\theta_n$

M : number of users \triangleright Same number of beams
 θ_n : Choose common steering angle of M beams
 $p = 1$: First codeword index
 $p = M$: Last codeword index
while $p \leq M$ **do**
 Determine focal distances f_0 using (27).
 Create steering vector for p^{th} beam using (31)
 Fill in the p^{th} codebook entry
end while

interference. However, when the users reside in the same LoS with the Tx, multiple access becomes challenging, as all beams have to be co-linear. The latter scenario is therefore particularly interesting and will be considered in the following examples.

A. NF-SDMA DESIGN AND ASSOCIATED BEAMS

Consider the scenario where six users reside within the range 2.5 m – 20 m along the direction $\theta_r = 0^\circ$. To design six orthogonal focused beams in order to simultaneously serve all users, we will use the codebook $CB\theta_n$, which is relevant for beams with $w_\theta = 0$ and $w_f \neq 0$. As reference we choose $\theta_{r,ref} = 0^\circ$ and $f_{0,ref} \rightarrow \infty$, and all beams belonging to the codebook are characterized by $\theta_r = 0^\circ$ and focal distances given by (27). For a UPA with $N_x = N_y = 500$ elements, the first six beams are characterized by $f_{0,1} = 15.63$ m, $f_{0,2} = 7.81$ m, $f_{0,3} = 5.21$ m, $f_{0,4} = 3.91$ m, $f_{0,5} = 3.13$ m, $f_{0,6} = 2.60$ m. The beams that correspond to these focal distances are numerically propagated both for the circular UPA and the rectangular UPA, as shown in Fig. 6(a) and Fig. 6(b), respectively, where cross sections along the center of each beam ($x = y = 0$) are presented. The range of interest is divided into six zones (alternate white/gray areas), the boundaries of which are defined as the distances where the shown cross sections of neighboring beams acquire the same power density. As such, each user is located within each one of the six zones, and all users are served individually and simultaneously by the six focused beams.

For circular UPA, the maximum of each beam is co-located with minima of all the other beams, which are suppressed by more than 40 dB in all cases, essentially corresponding to power nulls. Note how, with decreasing distance, the minima become less suppressed, as a consequence of the fact that the approximation $d_{m1} = d_{m2} = \dots = d_{mN} \approx d_R$ in (6) gradually

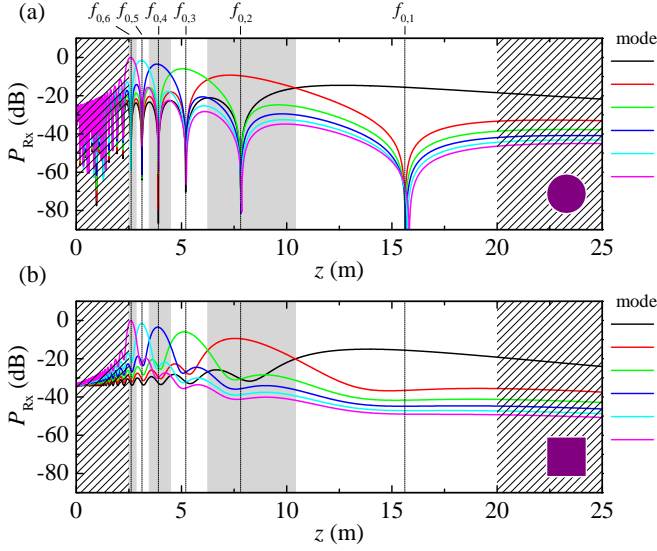


Figure 6. Local power distribution of focused beams and application to NF-SDMA. Six users reside within the range 2.5 m – 20 m, which is divided into six zones (alternate white/gray areas). Each user, located within each zone, is served by a dedicated focused beam according to the codebook $\text{CB}\theta_n$ with $\theta_n = 0^\circ$ for (a) circular and (b) rectangular UPA. The striped pattern marks the area outside the range of interest. All beams are normalized to the maximum of beam #6.

breaks. Note also that the maximum of each beam does not occur exactly at the corresponding f_0 , rather it is slightly shifted closer to the Tx. This is a well-known property of focused beams that has been studied analytically [14], [36] and is associated with how well focusing is performed; for larger footprints and/or smaller Tx-Rx distances, the beam maximum practically occurs at f_0 . Overall, for rectangular UPA, the minima are at substantially high power levels with respect to the maxima.

B. SPECTRAL EFFICIENCY

To evaluate the performance of NF-SDMA we use the receive signal-to-interference-plus-noise ratio (SINR) per Rx as performance metric, which is given by

$$\text{SINR}_m = \frac{P_m}{\sum_{l \neq m} P_l + P_v}, \quad (33)$$

where P_m is the received power at the m^{th} Rx and P_v is the noise power. The receive SINR at each Rx is related to its achievable rate as

$$R_m = \log_2(1 + \text{SINR}_m), \quad (34)$$

which can be used to express the overall spectral efficiency as $R = \sum_m R_m$.

First, the user locations are fixed within their corresponding zone, i.e. user #1 at $z = f_{0,1}$, user #2 at $z = f_{0,2}$, ..., user #6 at $z = f_{0,6}$. Using the beams of Fig. 6, the average spectral efficiency, $\langle R \rangle$, as a function of the SNR is demonstrated in Fig. 7(a), for both circular and rectangular UPAs. For low SNR, the nulls of focused beams generated with circular

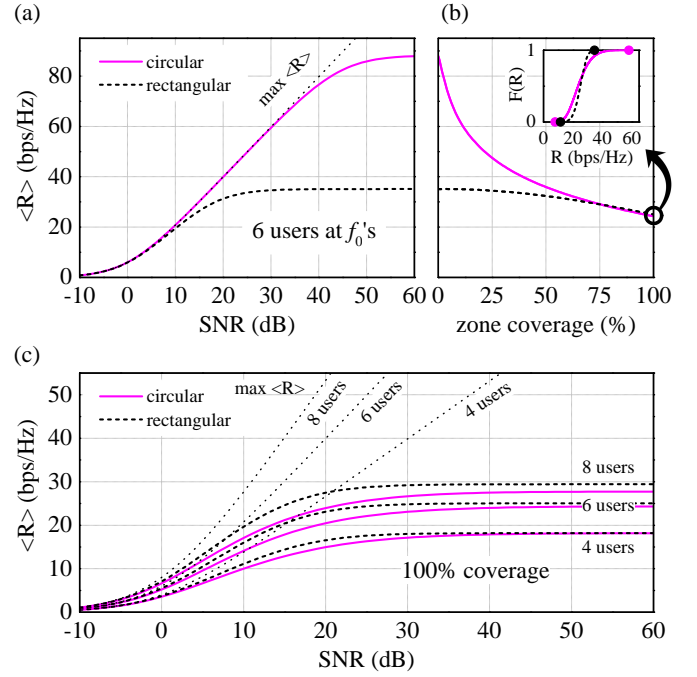


Figure 7. Spectral efficiency of the NF-SDMA scheme, presented in Fig. 6. (a) $\langle R \rangle$ as a function of the SNR, when each user is located at each f_0 , within its dedicated zone. (b) $\langle R \rangle$ as a function of the zone coverage, for SNR = 60 dB. inset: CDF for 100% zone coverage shown in (b). (c) $\langle R \rangle$ for 100% zone coverage, as a function of the SNR.

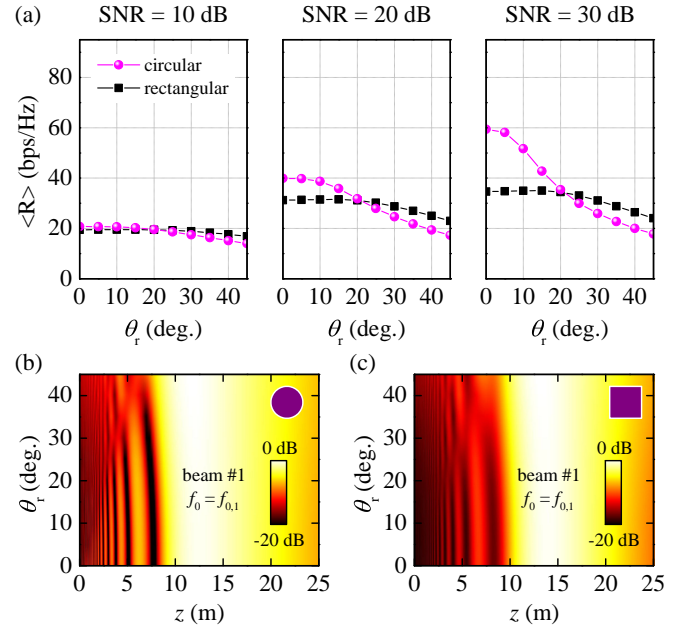


Figure 8. Spectral efficiency of the NF-SDMA scheme presented in Fig. 7(a), for users located beyond the broadside. (a) $\langle R \rangle$ as a function of the common direction θ_r for SNR = 10, 20, 30 dB. (b), (c) Cross-sections of beam #1 (shown in log scale), generated with circular and rectangular UPA, respectively.

UPAs are submerged in the noise background, yielding similar

performance to beams generated with rectangular UPAs. For higher SNR levels the performance of the former beams is dramatically enhanced, as the impact of noise is reduced, and the power nulling ability can be exploited more efficiently. The saturation of $\langle R \rangle$ at very high SNR levels results from subtle user offset from the power null locations. Overall, for a wide SNR range, the circular UPA approaches the upper bound of $\langle R \rangle$ (dashed line), which corresponds to zero interference.

For user locations that are not fixed, we may define the zone coverage as the fraction of each zone, within which each user can be located, around the individual reference location f_0 ; 0% coverage corresponds to users located at their individual f_0 , and 100% coverage corresponds to user locations covering fully each zone, thus spanning the entire 2.5 m – 20 m range. Fig. 7(b) shows $\langle R \rangle$ as a function of the zone coverage, for SNR = 60 dB. Note how, with increasing zone coverage, the performance of beams generated with circular UPA converges to that of beams generated with rectangular UPA. This is a direct consequence of the fact that circular UPAs generate focused beams with larger dynamic range between maxima and minima (nulls) than rectangular UPAs. Hence, averaging over all possible user locations leads to comparable average R between the two. However, the range of instantaneous values of R for each individual case differs substantially, as can be identified in the cumulative distribution functions (CDFs) shown in the inset of Fig. 7(b), which correspond to beams generated with the two UPAs, for 100% zone coverage.

In Fig. 7(c), $\langle R \rangle$ is studied as a function of the SNR, for 100% zone coverage. Similarly to the case of six users, for four users the 2.5 m – 20 m range is divided into four zones, and four focused beams are generated by the codebook, one assigned to each user/zone; similarly for eight users. In all cases, using either a circular or a rectangular UPA leads to similar performance, in accord with the conclusions of Fig. 7(b).

Returning to the scenario of Fig. 7(a), we now extend the study to users residing along a common direction with $\theta_r \neq 0^\circ$. In Fig. 8(a) we repeat the calculations of $\langle R \rangle$ for selected SNR levels, as a function of the angle θ_r , i.e. as the locations of all six users rotate around the Tx. As expected from the beam correlations previously presented in Fig. 4(b), with increasing angle the performance gradually degrades. The beams generated by circular UPAs outperform the respective generated by rectangular UPAs within a range of $\pm 20^\circ$, beyond which both beamsets deliver practically similar performance. An additional factor to the performance degradation is also the fact that, with increasing steering angle, the maxima and nulls are slightly shifted towards the Tx [14], as shown in Fig. 8(b),(c). As a result, their locations deviate from the locations of the Rx's, consequently leading to increased interference.

C. UPAs WITH QUANTIZED PHASE LEVELS

Typically, the phase in each UPA element is directly controlled by the driving currents. Therefore, the UPA elements can, in principle, acquire any phase within the entire $(-\pi, \pi)$ range. Having access to a prescribed (discrete) set of phases could be beneficial in terms of hardware complexity or performance

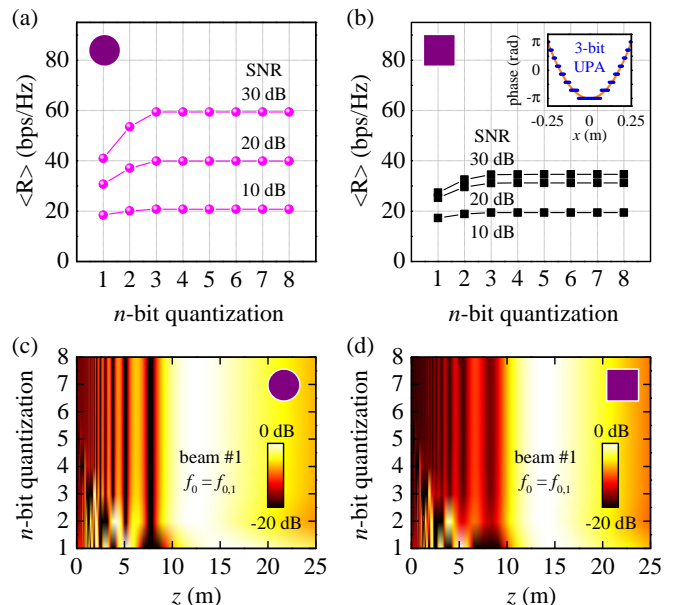


Figure 9. Impact of phase quantization on $\langle R \rangle$, for focused beams generated by an n -bit UPA. The scenario presented in Fig. 7(a) is examined here as a function of the UPA phase quantization levels, for (a) circular UPA and (b) rectangular UPA. Inset: Cross-section of UPA phase (blue dots), for a 3-bit UPA focusing towards $\theta_r = 0^\circ$, $f_0 = f_{0,1}$ (beam #1). The orange line is guide to the eye for the full (continuous) phase. (c),(d) Cross-sections of beam #1 (shown in log scale), generated with circular and rectangular UPA, respectively.

(e.g. latency). In this case, sampling the beam's footprint with a discrete set of phase levels is expected to have direct impact on the focusing efficiency and, consequently, on the associated performance.

Consider an n -bit UPA, i.e. an array that has access to only 2^n discrete phase levels within the continuous $(-\pi, \pi)$ range. In Fig. 9(a),(b) we repeat the calculations of $\langle R \rangle$ for such an array, as a function of the phase quantization levels. As intuitively expected, the performance improves with increasing n , quickly converging to the limit of the continuous phase, even with as few as 8 phase levels ($n = 3$). This behavior is observed for all SNR levels, beyond the selected examples, giving promise for efficient performance even with few discrete phase levels. An example of the quantized phase for a 3-bit UPA generating a focused beam towards $\theta_r = 0^\circ$, $f_0 = f_{0,1}$ (beam #1) is shown in the inset of Fig. 9(b). Our simulations reveal that low phase quantization results in distortion of the nulls and maxima, here shown in Fig. 9(c),(d) for beam #1. Increasing the discretization levels leads to improved focused beam formation and, consequently, to performance improvement.

VI. CONCLUSION

The design of NF-SDMA, based on focused beam generation with UPAs, has so far involved focused beams that are either entirely non-orthogonal or achieve orthogonality only asymptotically. In this work, we proposed the concept of using circular, instead of rectangular UPAs, to generate focused beams that have strictly zero correlations, thus enabling multiple access in the near-field with minimum interference. We

demonstrated analytically that such beams satisfy the orthogonality condition for finite-size transmitters, and we proposed codebook designs, which we evaluated in different scenarios. Our simulation results verified that the spectral efficiency of NF-SDMA schemes based on the proposed beams can be significantly higher than that achieved by focused beams generated with rectangular arrays. In the worst-case scenario, where all focused beams are co-linear and their spatial overlap is maximized, we found that the spectral efficiency using the proposed beams is superior to that achieved using focused beams generated by rectangular UPAs. With our work, we aim to bring the merits of classical far-field SDMA to the near-field, for 6G wireless connectivity and beyond.

APPENDIX

A. CHANNEL MODELING CONSISTENT WITH ANTENNA THEORY AND NUMERICAL PROPAGATION OF BEAMS IN FREE-SPACE

Consider a Tx equipped with a directional antenna that radiates total power P_{rad} . The E -field at the Rx, which is at distance d from the Tx, is

$$E_{\text{Rx}} = \sqrt{2Z_0 S_r} \exp(-jkd) \exp(j\phi), \quad (35)$$

where $S_r \equiv |E_{\text{Rx}}|^2 / 2Z_0$ is the power density of the Tx-radiated field at the Rx location, ϕ is the phase of the field at the Tx and Z_0 is the free-space wave impedance. Using the Tx antenna gain, G_t , and its (normalized) radiation pattern, $U_t(\theta, \phi)$, the power density at the Rx can be expressed as [37]

$$S_r = G_t U_t \frac{P_{\text{rad}}}{4\pi d^2}. \quad (36)$$

Hence, the E -field at the Rx is written as

$$E_{\text{Rx}} = \frac{\exp(-jkd)}{d} A \exp(j\phi), \quad (37)$$

with $A = \sqrt{2Z_0 G_t U_t P_{\text{rad}} / 4\pi}$, or simply

$$E_{\text{Rx}} = hw, \quad (38)$$

where

$$h = \frac{\exp(-jkd)}{d} \quad (39)$$

and

$$w = A \exp(j\phi). \quad (40)$$

For a Tx equipped with N antennas, each located at distance d_n from the Rx, with $n = 1, 2, \dots, N$, the E -field at the Rx results from the superposition of the individual fields from all antennas, i.e.

$$E_{\text{Rx}} = \sum_n h_n w_n, \quad (41)$$

where

$$h_n = \frac{\exp(-jkd_n)}{d_n} \quad (42)$$

and

$$w_n = A_n \exp(j\phi_n), \quad (43)$$

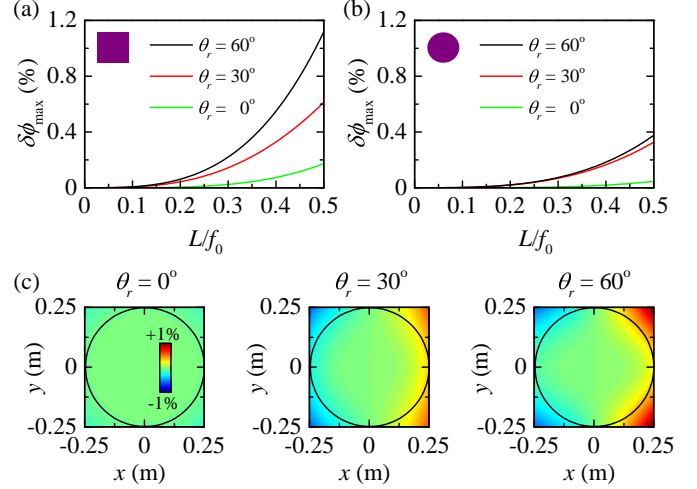


Figure 10. Relative error between the parabolic phase approximation (11) and the exact spherical phase (2). (a), (b) $\delta\phi_{\text{max}}$ for rectangular and circular UPA, respectively. (c) $\delta\phi(x, y)$ for $f_0 = 1$ m and $\theta_r = 0^\circ, 30^\circ, 60^\circ$. The inner circle and outer square outline the boundary of the circular UPA and rectangular UPA, respectively.

in which A_n and ϕ_n is the amplitude and phase, respectively, of the n^{th} antenna element of the Tx. This model is applicable from the radiating near-field up to the far-field of the Tx antennas. Using (41), (42), (43) with ϕ_n given by (2) (calculated at the n^{th} UPA element location) we numerically calculate the radiated E -field in space, as a function of the Rx location. In the figures, we plot the $|E|^2$, which corresponds to the local power density, yielding the beam propagation profiles in free-space.

B. FAR-FIELD ORTHOGONALITY

For a Rx in the far-field, (8) can be approximated as

$$\psi_n \approx k \left(d_R - \frac{x_m}{d_R} x_n \right) = kd_R - k \sin \theta_R x_n, \quad (44)$$

where the location of the Rx is $(x_m = d_R \sin \theta_R, y_m = 0, z_m = d_R \cos \theta_R)$, $d_R = \sqrt{x_m^2 + y_m^2 + z_m^2}$, and θ_R is the Tx-Rx angle. Similarly, (9) can be approximated as

$$\phi_n \approx kf_0 - k \sin \theta_R x_n. \quad (45)$$

Note that ψ_n in (44) and ϕ_n (45) have identical functional form and, hence, the reasoning followed for focused beams in Sec. III-B can be similarly applied, to conclude that the angular orthogonality of the steering vectors guarantees that a maximum of one beam will be located at a null of another beam, in the angular domain. This is exactly the well-known property of classical far-field SDMA.

C. VALIDITY RANGE OF PARABOLIC PHASE APPROXIMATION

In this section we demonstrate that the parabolic phase approximation given by (11) is valid for a wide range of values

for the UPA size L , the focal distance f_0 and the steering angle θ_r . To this end, we define the relative phase error

$$\delta\phi(x, y) = \frac{\phi_{\text{exact}}(x, y) - \phi_{\text{approx}}(x, y)}{\phi_{\text{exact}}(x, y)} 100\%, \quad (46)$$

where $\phi_{\text{exact}}(x, y)$ accounts for the exact spherical phase (2) and $\phi_{\text{approx}}(x, y)$ for the approximation (11). Because $\delta\phi(x, y)$ varies on the surface of the UPA, we define the maximum error $\delta\phi_{\text{max}}$, as the maximum value of $|\delta\phi(x, y)|$.

In Fig. 10(a),(b) we plot $\delta\phi_{\text{max}}$ for a rectangular and circular UPA, respectively, as a function of the ratio L/f_0 . While, with increasing steering angle, $\delta\phi_{\text{max}}$ increases, it remains practically below 1% for $L/f_0 < 0.5$, i.e. for focal distance larger than $f_0 > 2L$.

In Fig. 10(c) we plot $\delta\phi(x, y)$, for the three steering angles examined in Fig. 10(a),(b), using a UPA with $N_x = N_y = 500$ elements. The outer square outlines the boundary of the rectangular UPA, while the inner circle outlines the boundary of the circular UPA. As a worst-case scenario, a short focal distance is considered, i.e. $f_0 = 1$ m, so that the plots correspond to the largest error observed for $L/f_0 = 0.5$. These plots reveal the origin of the different $\delta\phi_{\text{max}}$ values between the two UPAs; the maximum error is accumulated towards the corners of the square area and is therefore excluded when considering the inner circular area.

D. BEAM CORRELATIONS FOR RECTANGULAR UPA

For rectangular UPA, integration of (12) leads to the general result

$$C_{\text{rect}}(w_\theta, w_f) = \frac{\pi l_x l_y}{L_x L_y w_f} \times |\text{erf}(q_x + q_z) + \text{erf}(q_x - q_z)| |\text{erf}(q_y)|, \quad (47)$$

where the parameters q_x, q_y, q_z are given by

$$q_x = \frac{1+j}{4} \frac{L_x}{l_x} \sqrt{w_f \delta_\theta}, \quad (48a)$$

$$q_y = \frac{1+j}{4} \frac{L_y}{l_y} \sqrt{w_f}, \quad (48b)$$

$$q_z = \frac{1+j}{2} \frac{w_\theta}{\sqrt{w_f \delta_\theta}}. \quad (48c)$$

For small angles, $w_\theta \rightarrow 0$, $\delta_\theta \rightarrow 1$, and (47) reduces to (19), using the substitutions $L_x \rightarrow N_x l_x$ and $L_y \rightarrow N_y l_y$.

ACKNOWLEDGMENT

This work was supported by the European Commission's Horizon Europe Programme under the Smart Networks and Services Joint Undertaking through TERA6G Project under Grant 101096949 and through INSTINCT Project under Grant 101139161.

REFERENCES

- [1] R. Roy, "Spatial division multiple access technology and its application to wireless communication systems," in *1997 IEEE 47th Vehicular Technology Conference. Technology in Motion*, vol. 2, 1997, pp. 730–734 vol.2.
- [2] "ITU recommendation m.2160," <https://www.itu.int/rec/R-REC-M.2160/en>.
- [3] H. Tataria, M. Shafi, A. F. Molisch, M. Dohler, H. Sjöland, and F. Tufvesson, "6G wireless systems: Vision, requirements, challenges, insights, and opportunities," *Proceedings of the IEEE*, vol. 109, no. 7, pp. 1166–1199, 2021.
- [4] C. Han, Y. Chen, L. Yan, Z. Chen, and L. Dai, "Cross far- and near-field wireless communications in terahertz ultra-large antenna array systems," *IEEE Wireless Communications*, vol. 31, no. 3, pp. 148–154, 2024.
- [5] X. Pei, H. Yin, L. Tan, L. Cao, Z. Li, K. Wang, K. Zhang, and E. Björnson, "RIS-aided wireless communications: Prototyping, adaptive beamforming, and indoor/outdoor field trials," *IEEE Transactions on Communications*, vol. 69, no. 12, pp. 8627–8640, 2021.
- [6] W. Tang, M. Z. Chen, X. Chen, J. Y. Dai, Y. Han, M. D. Renzo, Y. Zeng, S. Jin, Q. Cheng, and T. J. Cui, "Wireless communications with reconfigurable intelligent surface: Path loss modeling and experimental measurement," *IEEE Transactions on Wireless Communications*, vol. 20, no. 1, pp. 421–439, Jan 2021.
- [7] A. Singh, A. J. Alqaraghuli, and J. M. Jornet, "Wavefront engineering at terahertz frequencies through intelligent reflecting surfaces," in *2022 IEEE 23rd International Workshop on Signal Processing Advances in Wireless Communication (SPAWC)*, 2022, pp. 1–5.
- [8] F. Ahmed, T. Hassan, N. Melouki, H. Naseri, P. PourMohammadi, A. Iqbal, and T. A. Denidni, "A multibit and frequency-reconfigurable reflecting surface for RIS applications," *IEEE Antennas and Wireless Propagation Letters*, vol. 23, no. 2, pp. 653–657, 2024.
- [9] V. Arun and H. Balakrishnan, "RFocus: Beamforming using thousands of passive antennas," in *17th USENIX Symposium on Networked Systems Design and Implementation (NSDI 20)*. Santa Clara, CA: USENIX Association, feb 2020, pp. 1047–1061. [Online]. Available: <https://www.usenix.org/conference/nsdi20/presentation/arun>
- [10] M. Cui and L. Dai, "Channel estimation for extremely large-scale MIMO: Far-field or near-field?" *IEEE Transactions on Communications*, vol. 70, no. 4, pp. 2663–2677, 2022.
- [11] P. Ramezani and E. Björnson, *Near-Field Beamforming and Multiplexing Using Extremely Large Aperture Arrays*. Cham: Springer International Publishing, 2024, pp. 317–349. [Online]. Available: <https://doi.org/10.1007/978-3-031-37920-8>
- [12] A. Singh, V. Petrov, H. Guerboukha, I. V. Reddy, E. W. Knightly, D. M. Mittleman, and J. M. Jornet, "Wavefront engineering: Realizing efficient terahertz band communications in 6G and beyond," *IEEE Wireless Communications*, pp. 1–7, 2023.
- [13] G. Stratidakis, S. Droulias, and A. Alexiou, "Beam-forming and beam-focusing capabilities in RIS-aided communications," in *2023 IEEE Future Networks World Forum (FNWF)*, 2023, pp. 1–5.
- [14] S. Droulias, G. Stratidakis, and A. Alexiou, "Near-field engineering in RIS-aided links: Beamfocusing analytical performance assessment," *IEEE Access*, vol. 12, pp. 29 536–29 546, 2024.
- [15] G. Stratidakis, S. Droulias, and A. Alexiou, "Perceptive, resilient, and efficient networks: Programming the wireless environment with reconfigurable intelligent surfaces," *IEEE Vehicular Technology Magazine*, pp. 2–9, 2024.
- [16] S. Droulias, G. Stratidakis, and A. Alexiou, "Bending beams for 6G near-field communications," *IEEE Transactions on Wireless Communications*, vol. 24, no. 2, pp. 1467–1480, 2025.
- [17] C. Huang, A. Zappone, G. C. Alexandropoulos, M. Debbah, and C. Yuen, "Reconfigurable intelligent surfaces for energy efficiency in wireless communication," *IEEE Transactions on Wireless Communications*, vol. 18, no. 8, pp. 4157–4170, 2019.
- [18] M. Ahsan, S. Jamil, M. T. Ejaz, and M. S. Abbas, "Energy efficiency maximization in RIS-assisted wireless networks," in *2021 International Conference on Computing, Electronic and Electrical Engineering (ICE Cube)*, 2021, pp. 1–6.
- [19] N. M. Tran, M. M. Amri, J. H. Park, D. I. Kim, and K. W. Choi, "Reconfigurable-intelligent-surface-aided wireless power transfer systems: Analysis and implementation," *IEEE Internet of Things Journal*, vol. 9, no. 21, pp. 21 338–21 356, 2022.
- [20] Z. Yang, M. Chen, W. Saad, W. Xu, M. Shikh-Bahaei, H. V. Poor, and S. Cui, "Energy-efficient wireless communications with distributed reconfigurable intelligent surfaces," *IEEE Transactions on Wireless Communications*, vol. 21, no. 1, pp. 665–679, 2022.
- [21] H. Zhang, N. Shlezinger, F. Guidi, D. Dardari, M. F. Imani, and Y. C. Eldar, "Near-field wireless power transfer for 6G internet of everything mobile networks: Opportunities and challenges," *IEEE Communications Magazine*, vol. 60, no. 3, pp. 12–18, 2022.
- [22] Z. Li, J. Zhang, J. Zhu, and L. Dai, "RIS energy efficiency optimization with practical power models," in *2023 International Wireless Communications and Mobile Computing (IWCMC)*, 2023, pp. 1172–1177.

- [23] H. Wymeersch, J. He, B. Denis, A. Clemente, and M. Juntti, "Radio localization and mapping with reconfigurable intelligent surfaces: Challenges, opportunities, and research directions," *IEEE Vehicular Technology Magazine*, vol. 15, no. 4, pp. 52–61, 2020.
- [24] J. He, F. Jiang, K. Keykhosravi, J. Kokkonen, H. Wymeersch, and M. Juntti, "Beyond 5G RIS mmwave systems: Where communication and localization meet," *IEEE Access*, vol. 10, pp. 68 075–68 084, 2022.
- [25] H. Zhang, B. Di, K. Bian, Z. Han, H. V. Poor, and L. Song, "Toward ubiquitous sensing and localization with reconfigurable intelligent surfaces," *Proceedings of the IEEE*, vol. 110, no. 9, pp. 1401–1422, 2022.
- [26] T. Ma, Y. Xiao, X. Lei, L. Zhang, Y. Niu, and G. K. Karagiannidis, "Reconfigurable intelligent surface-assisted localization: Technologies, challenges, and the road ahead," *IEEE Open Journal of the Communications Society*, vol. 4, pp. 1430–1451, 2023.
- [27] S. Droulias, G. Stratidakis, and A. Alexiou, "Orthogonal beams and codebook design for near-field space division multiple access in 6G systems," *IEEE Transactions on Antennas and Propagation*, pp. 1–1, 2025.
- [28] N. Decarli and D. Dardari, "Communication modes with large intelligent surfaces in the near field," *IEEE Access*, vol. 9, pp. 165 648–165 666, 2021.
- [29] J. Zuo, X. Mu, and Y. Liu, "Near-field non-orthogonal multiple access communications," in *GLOBECOM 2023 - 2023 IEEE Global Communications Conference*, 2023, pp. 649–654.
- [30] Z. Wu and L. Dai, "Multiple access for near-field communications: SDMA or LDMA?" *IEEE Journal on Selected Areas in Communications*, vol. 41, no. 6, pp. 1918–1935, 2023.
- [31] M. Cui, Z. Wu, Y. Lu, X. Wei, and L. Dai, "Near-field MIMO communications for 6G: Fundamentals, challenges, potentials, and future directions," *IEEE Communications Magazine*, vol. 61, no. 1, pp. 40–46, 2023.
- [32] C. Ouyang, Z. Wang, Y. Chen, X. Mu, and P. Zhu, "A primer on near-field communications for next-generation multiple access," *Proceedings of the IEEE*, pp. 1–39, 2024.
- [33] Z. Wu, M. Cui, and L. Dai, "Enabling more users to benefit from near-field communications: From linear to circular array," *IEEE Transactions on Wireless Communications*, vol. 23, no. 4, pp. 3735–3748, 2024.
- [34] G. Torcolacci, N. Decarli, and D. Dardari, "Holographic MIMO communications exploiting the orbital angular momentum," *IEEE Open Journal of the Communications Society*, vol. 4, pp. 1452–1469, 2023.
- [35] L. Froehly, F. Courvoisier, A. Mathis, M. Jacquot, L. Furfaro, R. Giust, P. A. Lacourt, and J. M. Dudley, "Arbitrary accelerating micron-scale caustic beams in two and three dimensions," *Opt. Express*, vol. 19, no. 17, pp. 16 455–16 465, Aug 2011. [Online]. Available: <https://opg.optica.org/oe/abstract.cfm?URI=oe-19-17-16455>
- [36] S. Droulias and A. Alexiou, "Reconfigurable intelligent surface: an angular spectrum representation approach," in *2022 56th Asilomar Conference on Signals, Systems, and Computers*, 2022, pp. 413–418.
- [37] —, "Reconfigurable intelligent surface: MIMO or radiating sheet?" *IEEE Transactions on Wireless Communications*, vol. 23, no. 4, pp. 2726–2739, 2024.